

Zinc-Blende group III-V/ group IV epitaxy: importance of the miscut Supplemental Materials

C. Cornet^{1,*}, S. Charbonnier², I. Lucci¹, L. Chen¹, A. Létoublon¹, A. Alvarez¹, K. Tavernier¹, T. Rohel¹,
R. Bernard¹, J.-B. Rodriguez⁴, L. Cerutti⁴, E. Tournié⁴, Y. Léger¹, M. Bahri⁵, G. Patriarche⁵, L.
Largeau⁵, A. Ponchet³, P. Turban² and N. Bertru¹

¹Univ Rennes, INSA Rennes, CNRS, Institut FOTON – UMR 6082, F-35000
Rennes, France

²Univ Rennes, CNRS, IPR (Institut de Physique de Rennes) - UMR 6251, F-35000 Rennes, France

³CEMES-CNRS, Université de Toulouse, UPS, 29 rue Jeanne Marvig, BP 94347 Toulouse
Cedex 04, France

⁴IES, Univ. Montpellier, CNRS, Montpellier, France

⁵Université Paris-Saclay, CNRS, Centre de Nanosciences et de Nanotechnologies, 91120, Palaiseau, France

DETERMINATION OF THE CRITICAL MISCUT

At the beginning of III-V/Si crystal growth, 3D III-V islands are formed at the Si surface. The surface density of these islands is usually directly inferred from direct Atomic Force Microscopy or Transmission Electron Microscopy techniques. From this value, one can directly determine the average distance between two islands. Here, the situation is different, as determining the critical miscut requires the knowledge of the average distance between islands in a specific crystallographic direction (e.g. the [110] one), corresponding to the miscut direction. In the following, the formation of stable III-V nuclei at the Si surface are considered as independent and random in space (as a first approximation). A description of III-V islands surface distribution can thus be given by using the Poisson distribution. Therefore, considering d to be the surface density of islands, the probability to be at a distance r of an island in \mathbb{R}^2 is:

$$P(r) = 2\pi r d e^{-d\pi r^2} \quad (1)$$

The mathematical expectation in \mathbb{R}^2 is obtained by averaging this value over r , and gives the mean distance between two islands:

$$d_{moy} = \int_0^\infty P(r) r dr = 2\pi d \int_0^\infty e^{-d\pi r^2} r^2 dr \quad (2)$$

By integration, it comes:

$$d_{moy} = \frac{1}{2\sqrt{d}} \quad (3)$$

If we consider two islands aligned toward a direction having an angle θ with the miscut direction, the average distance along the miscut direction is therefore:

$$d_{1D,\theta} = d_{moy} |\cos \theta| \quad (4)$$

Finally, assuming a perfectly isotropic in-plane island distribution (corresponding to experimental observations), one can average this value over all the θ angles between 0 and 2π , in order to get the mean distance between 2 islands in 1D :

$$d_{1D} = \frac{1}{2\pi} \int_0^\infty d_{moy} |\cos \theta| d\theta = \frac{1}{\pi\sqrt{d}} \quad (5)$$

GROWTH AND MICROSCOPY DETAILS

GaSb/AlSb/Si sample presented in Fig. 2(a&b):

The 0.3°-off and 6°-off (001) Si substrates were first prepared *ex situ* according to the procedure described in ref. [1] before being loaded into the MBE reactor. The substrate temperature was then ramped up to 800 °C at ~ 20 °C/min and then immediately cooled at the same rate down to 450 °C, without any intentional flux (all shutter cells being kept closed). MBE growth was initiated by simultaneous opening of Al and Sb shutters to grow 4 monolayers (MLs) of AlSb followed by a 5 nm thick GaSb layer. Next the temperature was ramped to 500 °C to grow a 500 nm thick GaSb layer. Three-period (5 nm GaSb/1 ML AlSb) marker superlattices were inserted after growth of 5 nm, 50 nm, 100 nm, 200 nm GaSb to track the evolution of the growth throughout the structure. These marker superlattices can be seen at large magnification on Figs. 2 a) and 2 b). The temperatures were measured by a pyrometer, and the growth rates were 0.35 ML/s for AlSb and 0.65 ML/s for GaSb.

GaP/Si sample presented in Fig. 2(c&d), Fig. 3(a):

GaP/Si samples presented in Fig. 2 (c&d) and Fig. 3(a) were grown by Molecular Beam Epitaxy (MBE) on a HF-

chemically prepared Si(001) substrate [2]. For all the samples, the substrate has been heated at 800°C during 10 minutes to remove hydrogen at the surface, and a 10-nm thick GaP/Si deposition was performed by Migration Enhanced Epitaxy at 350°C. Subsequently, successive 4 50nm-thick GaP layers were grown by conventional MBE growth mode at increasing growth temperature: 500°C, 535°C, 565°C, and 600°C. Each MBE layer was separated by a 2-nm-thin AlGaP marker grown at the same temperature as the following GaP layer.

GaP/Si sample presented in Fig. 2(c) was grown on a nominal Si(001) substrate, with a miscut given by the manufacturer at $[0\pm0.5^\circ]$. V/III Beam Equivalent Pressure (BEP) ratio was set to 11 during the growth.

GaP/Si sample presented in Fig. 2(d) was grown under the same condition as the sample presented in Fig. 2(c), but on a Si(001) substrate with 6° miscut towards $[110]$ direction. V/III Beam Equivalent Pressure (BEP) ratio was set to 11 during the growth.

GaP/Si sample presented in Fig. 3(a) was grown under the same condition as the sample presented in Fig. 2(d), on a Si(001) substrate with 6° miscut towards $[110]$ direction. But this time, V/III Beam Equivalent Pressure (BEP) ratio was set to 5.5 during the growth. Besides, after the MBE growth, an amorphous thick As capping layer was deposited on the GaP/Si(001) film at cryogenic temperature, allowing the transfer of the sample to the ultra-high vacuum STM chamber experiment, as already discussed in refs. [3,4].

Transmission Electron Microscopy image of Fig. 2(a,b, c and d), S1 and S2:

The GaSb/Si and GaP/Si samples have been observed in cross-sectional view by Scanning Transmission Electron Microscopy on an aberration corrected microscope Titan Themis 200. The thin foil has been prepared by FIB following the $\langle 110 \rangle$ zone axis (the $\langle 110 \rangle$ direction parallel to the surface steps linked to the 6° misorientation). The FIB preparation has been followed by a cleaning with argon milling at low voltage (1.5kV) during 9 minutes to remove the material redeposition (gallium and antimony) during the FIB process. Figures 2c, 2d, S1b, and S2 correspond to STEM Bright Field images. Figures 2a, 2b, S1.a and S1.c are Dark Field images recorded by using the (002) diffraction spot.

Histograms presented in Fig. 2 (c,d) have been drawn by counting by eyes the number, and sizes of antiphase domains observed in many TEM images. For the GaP grown on nominal (vicinal) Si substrate, TEM images examples are given in Fig. S1 (Fig. S2).

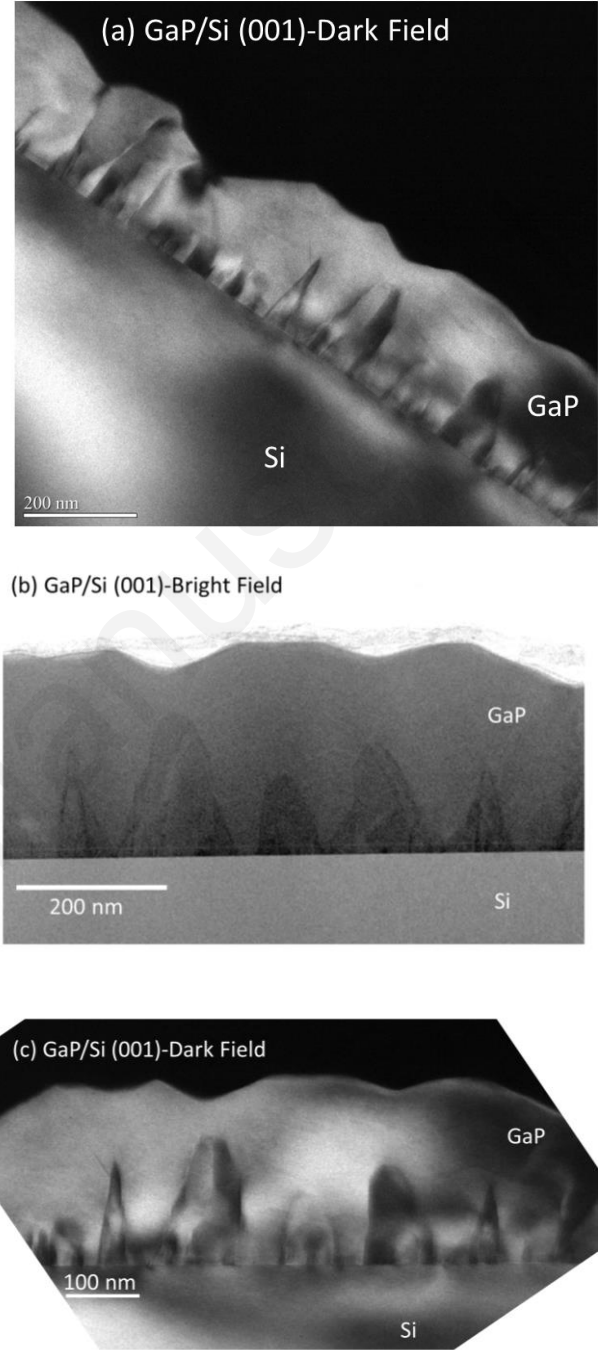


FIG. S1: Transmission Electron Microscopy images of the GaP/Si(001) sample previously described, with (a) the Dark field image of the sample over a $1\mu\text{m}$ range, (b) the bright field image corresponding to a smaller scale. (c) is the dark field image performed exactly in the same part of the sample than (b), showing the Antiphase Domains.

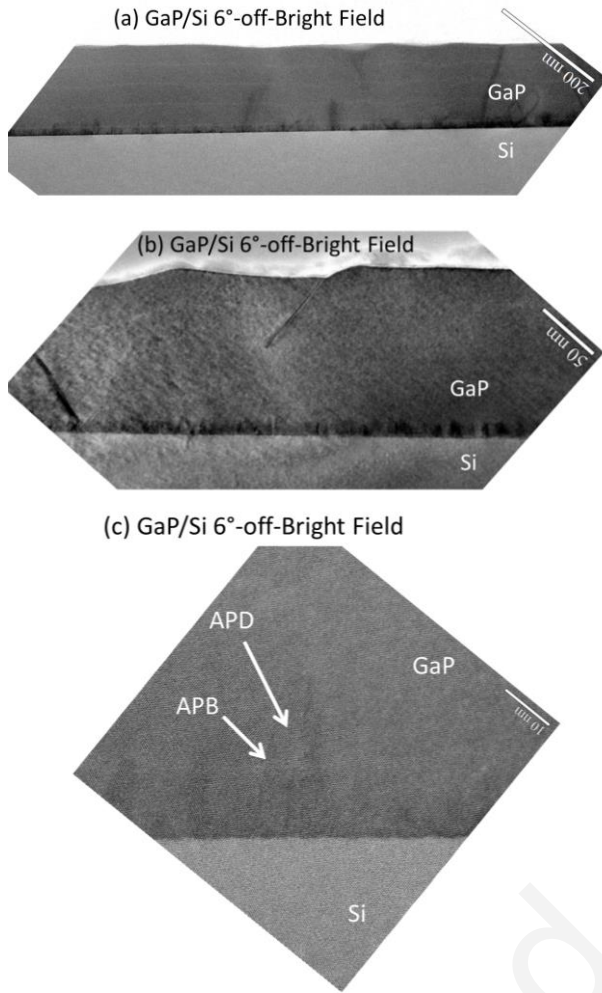


FIG. S2: Transmission Electron Microscopy images of the GaP/Si(001)-6°-off sample previously described, with the Bright-Field images at different scales (a) for a 800 nm lateral dimension, (b) with a 300 nm lateral dimension and (c) with a 60 nm lateral dimension.

Fig. S3 gives the dark-field TEM images of the GaSb/Si samples presented in fig. 2(a) and (b) of the manuscript. While in the first case (nominal substrate), antiphase boundaries emerge at the surface of the sample, it is not the case for the sample grown on 6°-off orientation. However, many other defects can be observed such as Micro-Twins or dislocations, which propagate through the layer.

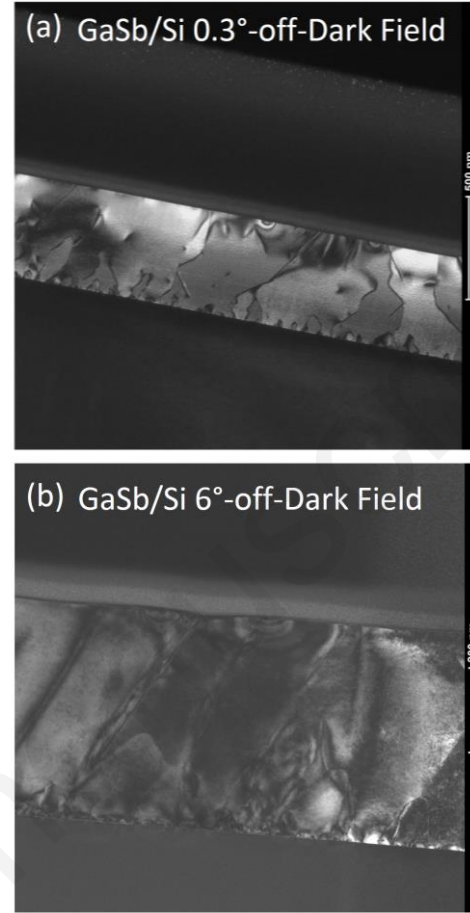


FIG. S3: Transmission Electron Microscopy images of the GaSb/Si(001) grown on (a) nominal substrate and (b) vicinal substrate under dark-field imaging conditions.

Scanning Tunneling Microscopy image of Fig. 3(a):

Scanning Tunneling Microscopy (STM) was performed at room-temperature in the constant current mode of operation. Tungsten electro-chemically etched tips were used. After introduction in the ultra-high vacuum STM chamber, the protective amorphous As layer was thermally desorbed at 500°C. Raw STM images were corrected by subtraction of a basal plane.

Scanning Tunneling Microscopy image presented in Fig. 3(a) used in the manuscript to explain the antiphase domain burying is extracted from a set of experiments on different samples showing the same behavior. Fig. S4 presents a 100*100 nm² STM image obtained on the same sample. The covering of one domain by the other is confirmed and the polarity of the two different domains can again be distinguished without any ambiguity. To check the validity and homogeneity of the process at large scale, Fig. S5(a) displays a 300*300nm² STM image of another part of the

sample, typically 1 centimeter away from the observation of Fig. 3(a), showing still the same surface structure. A $150 \times 150 \text{ nm}^2$ zoom on the lower left part of Fig. S5(a) is presented in Fig. S5(b). Here extended flat (001) facets are locally observed on two neighboring domains. At this scale, the GaP(001) surface reconstruction is clearly visible and allows unambiguous identification of the local III-V [-110] direction and thus the local polarity of both domains. The GaP domain having its [-110] direction parallel to the [110] direction of the Si substrate again coalesces over the other polarity in agreement with Fig. 3(a). A larger scale image on the same sample is also presented in Fig. S6 confirming the homogeneity of the process over the sample. Finally, these observations have been also made on other samples, as the GaP/Si one presented in Fig. S7, where atomic Force Microscopy on $5 \times 5 \text{ }\mu\text{m}^2$ and $10 \times 10 \text{ }\mu\text{m}^2$ reveals one more time the same surface morphology, corresponding to the moment where one polarity bury the other. Small inclusions of the minority polarity are still observed on these images.

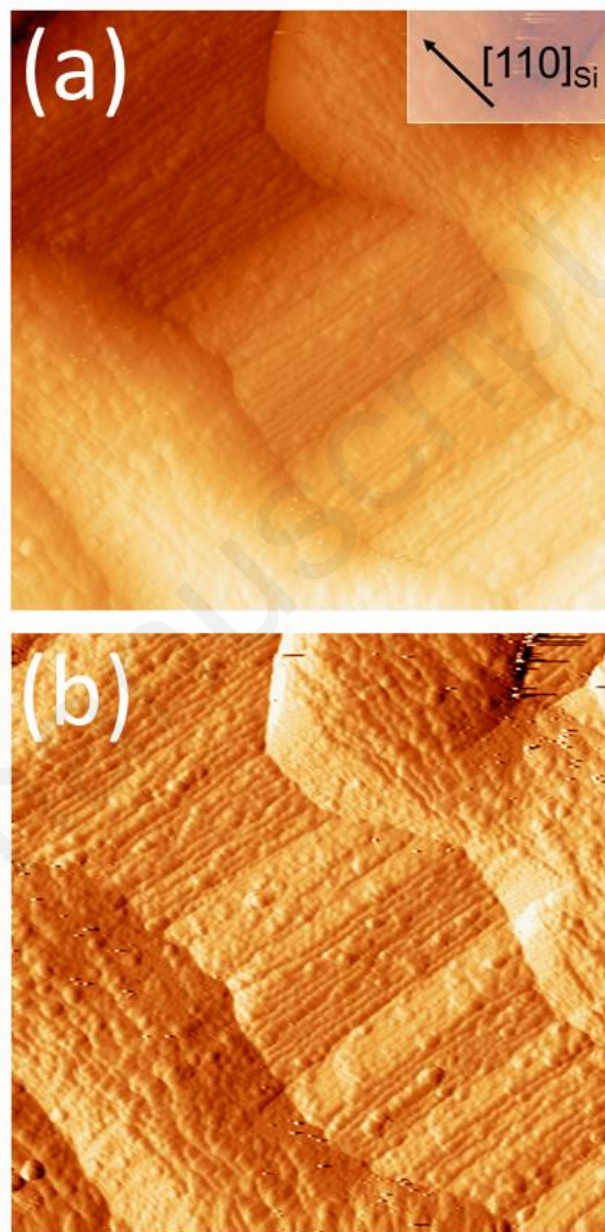


FIG. S4: $100 \times 100 \text{ nm}^2$ Scanning Tunneling Microscopy image of the GaP/Si-6°-off sample shown in the manuscript (fig. 3(a)), (a) topography and (b) derivative of the topography along scan direction, demonstrating the burying of one domain by the other one.

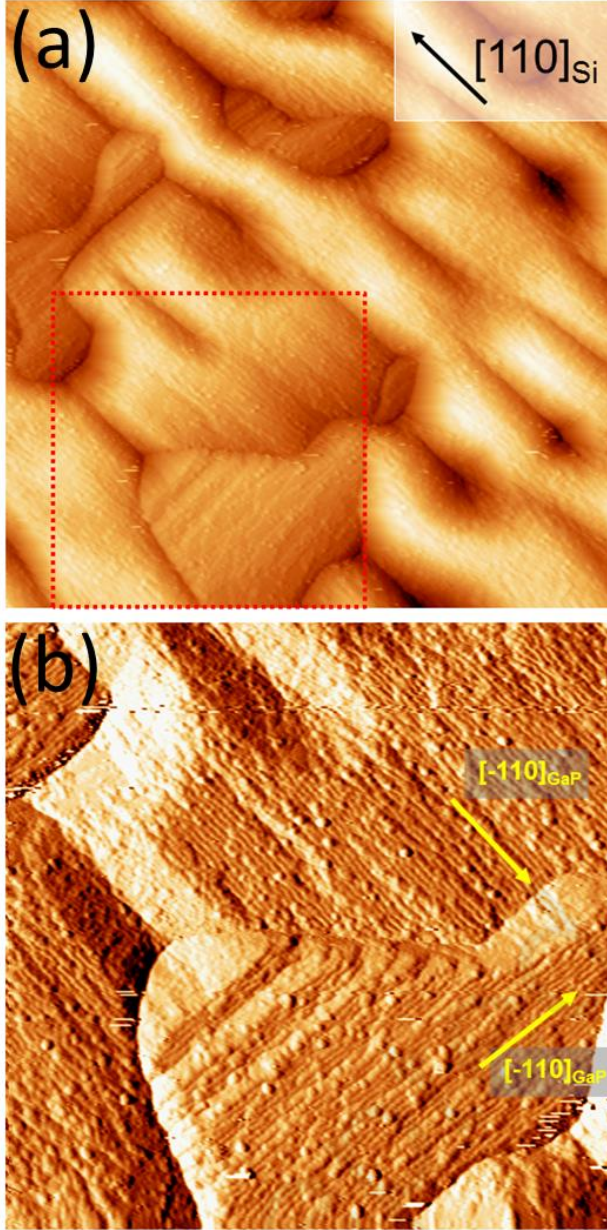


FIG. S5: (a) 300*300 nm² STM image of the GaP/Si-6°-off sample shown in the manuscript (fig. 3(a)), performed elsewhere in the sample, revealing the same burying process, along the same crystal direction. Vertical color scale: 0-13.5nm. (b) 150*150 nm² zoom in the region marked in (a). The presence of (001) summital facets on the emerging antiphase domains allows unambiguous determination of the local polarity. The STM image was derived along scan direction to enhance atomic contrasts. Green arrows indicate the local $[-110]$ GaP directions for the two antiphase domains.

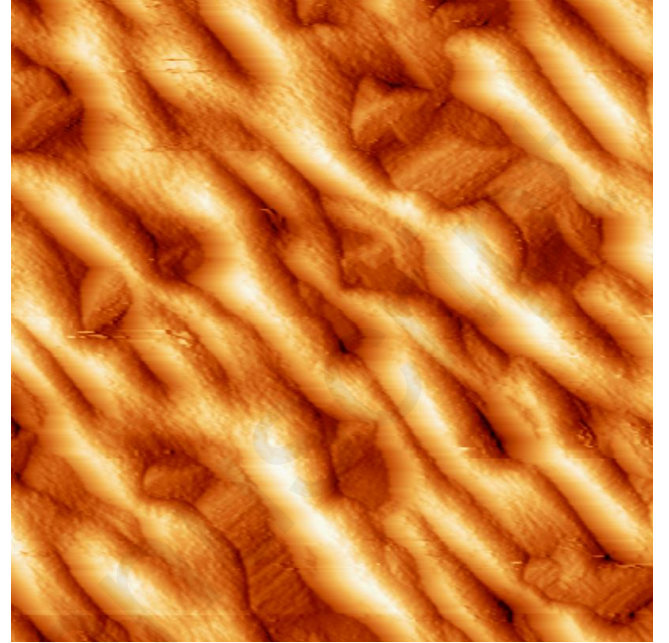


FIG. S6: 400*400 nm² Scanning Tunneling Microscopy image of the GaP/Si-6°-off sample shown in the manuscript (fig. 3(a)), revealing the same burying process at a larger scale, along the same crystal direction.

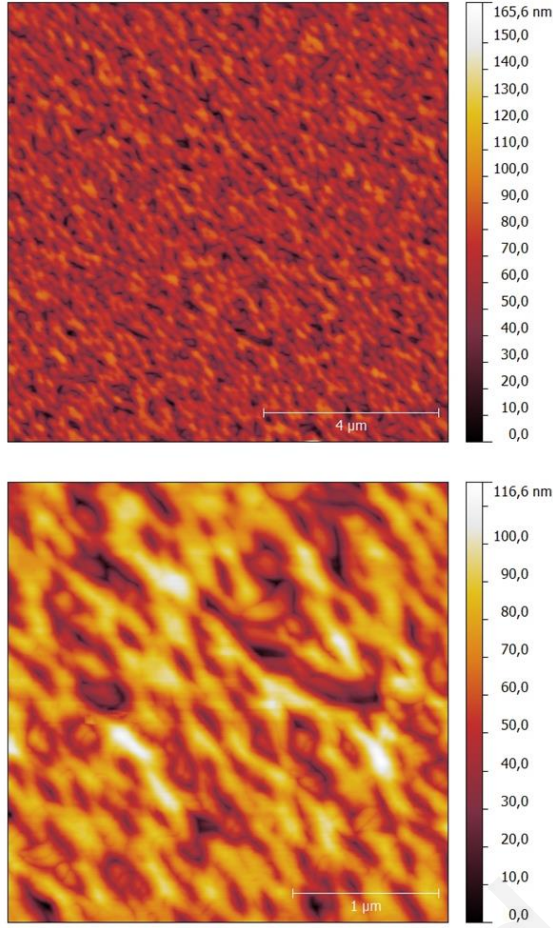


FIG. S7: Atomic Force Microscopy of another GaP/Si sample for which the burying process is ongoing. Anisotropy of the surface along the same direction can be seen on the $5 \times 5 \mu\text{m}^2$ image (a) and on the $10 \times 10 \mu\text{m}^2$ one.

BURYING OF THE ANTI-PHASE BY THE MAIN PHASE

As mentioned in the main article, the annihilation process is not strictly speaking an annihilation, but more a burying of one phase by the other, due to different growth rates of the different phases, thanks to the miscut. As it was also reported previously that stable facets may form where the APB emerges [5], an illustration of the APB propagation and APD burying is proposed in Fig. S8. But the real situation can be quite different from this picture, depending on the different materials systems, the relative stability of high angle facets, and their growth rate.

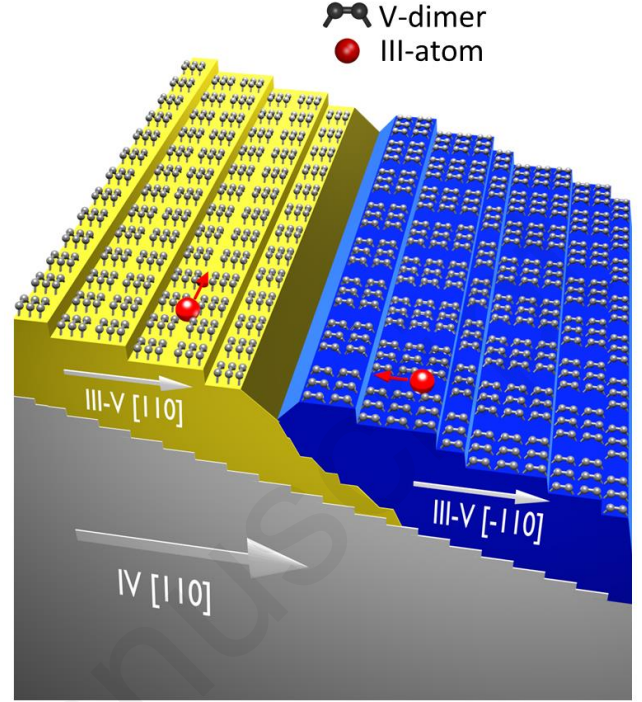


FIG. S8: Illustration of the burying process, and the propagation of the antiphase boundary when the growth rate imbalance coefficient is far from unity.

GROWTH RATE IMBALANCE COEFFICIENT

The determination of the growth rate imbalance coefficient is conditional upon knowing experimentally the growth rates or direct step incorporation rates per site of each surfaces A and B. Experimental determination of incorporation rates was proposed in the pioneering works of Shitara et al. for MBE-grown GaAs, by using reflection high-energy electron diffraction [6,7]. In these works, they determined the direct step incorporation rate per site R_I , which follows an Arrhenius dependency:

$$R_I = R_0 e^{-\frac{E_a}{k_B T}} \quad (2)$$

Therefore, the fitting of experimental data leads to the determination of a set of two parameters, which can be further extracted, namely E_a the activation energy, and R_0 the pre-factor. The parameters used in Fig. 4 have thus been determined from the work of Shitara et al. [6,7], especially for different V/III ratio. Table S1 gives these parameters:

Growth condition	Activation energy		Pre-factor	
	E_a (eV)		R_0 (atom.s ⁻¹ .site ⁻¹)	
	A	B	A	B
	surface	surface	surface	surface
V/III=2.0	4.10	1.96	$8.0.10^{23}$	$4.0.10^{11}$
V/III=2.5	3.89	1.41	$5.0.10^{22}$	$4.7.10^8$
V/III=4.3	2.63	1.02	$1.5.10^{15}$	$2.0.10^6$
V/III=6.8	1.50	0.87	$4.2.10^8$	$3.2.10^5$

Table S1: activation energies and pre-factors extracted from the fitting of experimental data from refs. [6,7] and used to plot Fig. 4 of the manuscript.

The imbalance coefficient was then determined as a function of the temperature and V/III ratio, with the values of Table S1.

- [1] K. Madiomanana, M. Bahri, J. B. Rodriguez, L. Largeau, L. Cerutti, O. Mauguin, A. Castellano, G. Patriarche, and E. Tournié, *J. Cryst. Growth* **413**, 17 (2015).
- [2] T. Quinci, J. Kuyyalil, T. N. Thanh, Y. P. Wang, S. Almosni, A. Létoublon, T. Rohel, K. Tavernier, N. Chevalier, O. Dehaese, N. Boudet, J. F. Bérar, S. Loualiche, J. Even, N. Bertru, A. L. Corre, O. Durand, and C. Cornet, *J. Cryst. Growth* **380**, 157 (2013).
- [3] C. Robert, C. Cornet, P. Turban, T. Nguyen Thanh, M. O. Nestoklon, J. Even, J. M. Jancu, M. Perrin, H. Folliot, T. Rohel, S. Tricot, A. Balocchi, D. Lagarde, X. Marie, N. Bertru, O. Durand, and A. Le Corre, *Phys. Rev. B* **86**, 205316 (2012).
- [4] I. Lucci, S. Charbonnier, L. Pedesseau, M. Vallet, L. Cerutti, J.-B. Rodriguez, E. Tournié, R. Bernard, A. Létoublon, N. Bertru, A. Le Corre, S. Rennesson, F. Semond, G. Patriarche, L. Largeau, P. Turban, A. Ponchet, and C. Cornet, *Phys. Rev. Mater.* **2**, 060401(R) (2018).
- [5] I. Lucci, S. Charbonnier, M. Vallet, P. Turban, Y. Léger, T. Rohel, N. Bertru, A. Létoublon, J.-B. Rodriguez, L. Cerutti, E. Tournié, A. Ponchet, G. Patriarche, L. Pedesseau, and C. Cornet, *Adv. Funct. Mater.* 1801585 (2018).
- [6] T. Shitara, J. Zhang, J. H. Neave, and B. A. Joyce, *J. Cryst. Growth* **127**, 494 (1993).
- [7] T. Shitara, J. Zhang, J. H. Neave, and B. A. Joyce, *J. Appl. Phys.* **71**, 4299 (1992).